

# *In vivo* three-dimensional spectroscopic photoacoustic imaging for monitoring nanoparticle delivery

Seungsoo Kim,<sup>1</sup> Yun-Sheng Chen,<sup>2</sup> Geoffrey P. Luke,<sup>2</sup> and Stanislav Y. Emelianov<sup>1,2,\*</sup>

<sup>1</sup>Department of Biomedical Engineering, University of Texas at Austin, Austin, TX, 78712, USA

<sup>2</sup>Department of Electrical and Computer Engineering, University of Texas at Austin, Austin, TX, 78712, USA

\*emelian@mail.utexas.edu

**Abstract:** *In vivo* monitoring of nanoparticle delivery is essential to better understand cellular and molecular interactions of nanoparticles with tissue and to better plan nanoparticle-mediated therapies. We developed a three-dimensional ultrasound and photoacoustic (PA) imaging system and a spectroscopic PA imaging algorithm to identify and quantify the presence of nanoparticles and other tissue constituents. Using the developed system and approach, three-dimensional *in vivo* imaging of a mouse with tumor was performed before and after intravenous injection of gold nanorods. The developed spectroscopic PA imaging algorithm estimated distribution of nanoparticle as well as oxygen saturation of blood. Moreover, silver staining of excised tumor tissue confirmed nanoparticle deposition, and showed good correlation with spectroscopic PA images. The results of our study suggest that three-dimensional ultrasound-guided spectroscopic PA imaging can monitor nanoparticle delivery *in vivo*.

© 2011 Optical Society of America

**OCIS codes:** (170.5120) Photoacoustic imaging; (110.7170) Ultrasound; (170.3880) Medical and biological imaging

---

## References and links

1. S. Mallidi, T. Larson, J. Tam, P. P. Joshi, A. Karpouk, K. Sokolov, and S. Emelianov, "Multiwavelength photoacoustic imaging and plasmon resonance coupling of gold nanoparticles for selective detection of cancer," *Nano Lett.* **9**(8), 2825–2831 (2009).
2. P. C. Li, C. R. Wang, D. B. Shieh, C. W. Wei, C. K. Liao, C. Poe, S. Jhan, A. A. Ding, and Y. N. Wu, "*In vivo* photoacoustic molecular imaging with simultaneous multiple selective targeting using antibody-conjugated gold nanorods," *Opt. Express* **16**(23), 18605–18615 (2008).
3. C. L. Bayer, Y. S. Chen, S. Kim, S. Mallidi, K. Sokolov, and S. Emelianov, "Multiplex photoacoustic molecular imaging using targeted silica-coated gold nanorods," *Biomed. Opt. Express* **2**(7), 1828–1835 (2011).
4. K. Homan, S. Kim, Y. S. Chen, B. Wang, S. Mallidi, and S. Emelianov, "Prospects of molecular photoacoustic imaging at 1064 nm wavelength," *Opt. Lett.* **35**(15), 2663–2665 (2010).
5. X. Huang, P. K. Jain, I. H. El-Sayed, and M. A. El-Sayed, "Plasmonic photothermal therapy (PPTT) using gold nanoparticles," *Lasers Med. Sci.* **23**(3), 217–228 (2008).
6. Y. S. Chen, W. Frey, S. Kim, K. Homan, P. Kruijzinga, K. Sokolov, and S. Emelianov, "Enhanced thermal stability of silica-coated gold nanorods for photoacoustic imaging and image-guided therapy," *Opt. Express* **18**(9), 8867–8878 (2010).
7. Y. S. Chen, W. Frey, S. Kim, P. Kruijzinga, K. Homan, and S. Emelianov, "Silica-coated gold nanorods as photoacoustic signal nanoamplifiers," *Nano Lett.* **11**(2), 348–354 (2011).
8. R. Shukla, V. Bansal, M. Chaudhary, A. Basu, R. R. Bhone, and M. Sastry, "Biocompatibility of gold nanoparticles and their endocytotic fate inside the cellular compartment: a microscopic overview," *Langmuir* **21**(23), 10644–10654 (2005).
9. S. Kim, Y.-S. Chen, G. P. Luke, M. Mehrmohammadi, J. R. Cook, and S. Y. Emelianov, "Ultrasound and photoacoustic image-guided photothermal therapy using silica-coated gold nanorods: in-vivo study," in *2010 IEEE Ultrasonics Symposium (IUS)*, (IEEE, 2010), pp. 233–236.
10. J. Shah, S. Park, S. Aglyamov, T. Larson, L. Ma, K. Sokolov, K. Johnston, T. Milner, and S. Y. Emelianov, "Photoacoustic imaging and temperature measurement for photothermal cancer therapy," *J. Biomed. Opt.* **13**(3), 034024 (2008).
11. X. Yang, S. E. Skrabalak, Z. Y. Li, Y. Xia, and L. V. Wang, "Photoacoustic tomography of a rat cerebral cortex *in vivo* with Au nanocages as an optical contrast agent," *Nano Lett.* **7**(12), 3798–3802 (2007).

12. M.-L. Li, J.-T. Oh, X. Xie, G. Ku, W. Wang, C. Li, G. Lungu, G. Stoica, and L. V. Wang, "Simultaneous molecular and hypoxia imaging of brain tumors *in vivo* using spectroscopic photoacoustic tomography," *Proc. IEEE* **96**(3), 481–489 (2008).
13. B. Wang, J. L. Su, J. Amirian, S. H. Litovsky, R. Smalling, and S. Emelianov, "Detection of lipid in atherosclerotic vessels using ultrasound-guided spectroscopic intravascular photoacoustic imaging," *Opt. Express* **18**(5), 4889–4897 (2010).
14. K. H. Song, C. Kim, K. Maslov, and L. V. Wang, "Noninvasive *in vivo* spectroscopic nanorod-contrast photoacoustic mapping of sentinel lymph nodes," *Eur. J. Radiol.* **70**(2), 227–231 (2009).
15. W. J. Akers, C. Kim, M. Berezin, K. Guo, R. Fuhrhop, G. M. Lanza, G. M. Fischer, E. Daltrozzi, A. Zumbusch, X. Cai, L. V. Wang, and S. Achilefu, "Noninvasive photoacoustic and fluorescence sentinel lymph node identification using dye-loaded perfluorocarbon nanoparticles," *ACS Nano* **5**(1), 173–182 (2011).
16. B. Nikoobakht and M. A. El-Sayed, "Preparation and growth mechanism of gold nanorods (NRs) using seed-mediated growth method," *Chem. Mater.* **15**(10), 1957–1962 (2003).
17. S. A. Prael, "Optical properties spectra compiled by Scott Prael," (retrieved 2009) <http://omlc.ogi.edu/spectral/>.
18. American National Standards Institute, *American National Standard for the Safe Use of Lasers*, ANSI Z136.1–2000 (ANSI, 2000).
19. R. A. Mucci, "A comparison of efficient beamforming algorithms," *IEEE Trans. Acoust. Speech Signal Process.* **32**(3), 548–558 (1984).
20. A. A. Oraevsky, S. L. Jacques, and F. K. Tittel, "Measurement of tissue optical properties by time-resolved detection of laser-induced transient stress," *Appl. Opt.* **36**(1), 402–415 (1997).
21. W.-F. Cheong, S. A. Prael, and A. J. Welch, "A review of the optical properties of biological tissues," *IEEE Quantum Electronics* **26**, 2166–2185 (1993).
22. Ref. [21] updated by W.-F. Cheong, further additions by L.V. Wang and S.L. Jacques, <http://omlc.ogi.edu/pubs/pdf/cheong90a.pdf>.
23. L. Wang, S. L. Jacques, and L. Zheng, "MCML--Monte Carlo modeling of light transport in multi-layered tissues," *Comput. Methods Programs Biomed.* **47**(2), 131–146 (1995).
24. L. Wang, S. L. Jacques, and L. Zheng, "CONV--convolution for responses to a finite diameter photon beam incident on multi-layered tissues," *Comput. Methods Programs Biomed.* **54**(3), 141–150 (1997).
25. S. Mallidi, T. Larson, J. Aaron, K. Sokolov, and S. Emelianov, "Molecular specific optoacoustic imaging with plasmonic nanoparticles," *Opt. Express* **15**(11), 6583–6588 (2007).
26. B. Wang, E. Yantsen, T. Larson, A. B. Karpiouk, S. Sethuraman, J. L. Su, K. Sokolov, and S. Y. Emelianov, "Plasmonic intravascular photoacoustic imaging for detection of macrophages in atherosclerotic plaques," *Nano Lett.* **9**(6), 2212–2217 (2009).

## 1. Introduction

Gold nanoparticles have been considered attractive contrast agents for photoacoustic molecular imaging [1–4], as well as therapeutic agents for photothermal therapy [5–7], because of high optical absorption properties, superior biocompatibility [8] and capability of molecular specific targeting of the cells. Monitoring of nanoparticle delivery is essential to better understand fundamental molecular pathways inside organisms and to better plan nanoparticle-mediated photothermal cancer therapy [9,10]. The photoacoustic (PA) imaging technique can detect nanoparticles (NPs) based on 2 ways: quantitative changes of PA signals between pre- and post-injection of NPs and spectroscopic methods.

Single-wavelength PA imaging has been used to detect contrast agents in live mice based on changes of PA signal intensity [2,11]. Unfortunately, analysis of PA signal at only one wavelength is prone to error because the increase of PA intensity can be caused not only by the deposition of contrast agents, but also by physiological changes (i.e., tumor growth, angiogenesis, etc.). Moreover, when longitudinal PA imaging is performed, the repeatability of the imaging experiments can be another problem because PA signals are linearly dependent with local laser fluence, which will be changed by tumor growth and re-positioning of the animal between imaging sessions. Multi-wavelength PA imaging (i.e., spectroscopic PA imaging) can be a solution to overcome the problems of single-wavelength PA imaging.

The spectroscopic PA imaging technique mainly relies on a tissue-dependent optical absorption spectrum. It can, therefore, distinguish different types of tissue such as oxyhemoglobin, deoxyhemoglobin, and lipid [12,13]. Spectroscopic PA imaging has also been used to detect NPs based on PA spectrum and NP absorption spectrum [1,14,15]. However, in order to utilize spectroscopic PA imaging for *in vivo* detection of NPs, a more robust imaging algorithm needs to be developed.

In this paper, we present an *in vivo* spectroscopic PA imaging algorithm as well as a three-dimensional (3-D) ultrasound (US) and PA imaging system. The developed system and

algorithm were used for the detection of polyethylene glycol (PEG)-coated (PEGylated) gold nanorods injected into the tail vein of a mouse bearing a subcutaneous tumor. The results of spectroscopic PA imaging before (i.e., control) and 31 hours after the NP injection showed that the developed system and algorithm can detect NPs *in vivo*. Moreover, silver staining of the excised tumor tissue confirmed the NP deposition, and showed good correlation with spectroscopic PA imaging results.

## 2. Materials and Methods

### 2.1. Nanoparticles

PEGylated gold nanorods (PEG-Au NRs) were synthesized for this study. First, cetyltrimethylammonium bromide (CTAB)-stabilized gold nanorods were prepared with a seed-mediated growth method [16]. Then the CTAB was replaced by mPEG-thiol through ligand exchange. The prepared PEG-Au NRs were characterized by ultraviolet-visible (UV-Vis) spectroscopy and transmission electron microscopy (TEM). The absorbance spectrum of PEG-Au NRs measured by UV-Vis spectroscopy is shown in Fig. 1, and compared with the absorption spectra of deoxyhemoglobin (Hb) and oxyhemoglobin (HbO<sub>2</sub>) reported in literature [17]. The wavelength of PEG-Au NRs' peak absorbance was about 790 nm, and the size of PEG-Au NRs, derived from the TEM image as shown in Fig. 1, was about 40 nm by 10 nm.

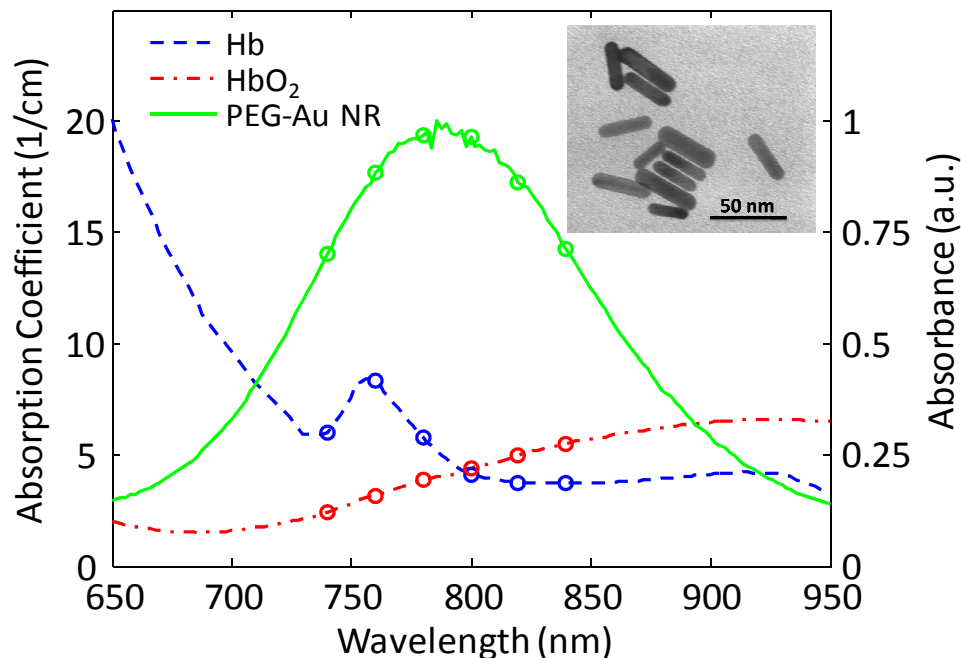


Fig. 1. The absorption spectra of deoxyhemoglobin (Hb, blue dashed line) and oxyhemoglobin (HbO<sub>2</sub>, red dash-dotted line) [17] compared to the absorbance spectrum of the PEGylated gold nanorod (PEG-Au NR, green solid line) measured by UV-Vis spectroscopy. Dots on each line correspond to wavelengths used for spectroscopic photoacoustic imaging. The transmission electron microscopy (TEM) image of PEG-Au NRs is also shown.

### 2.2. Mouse bearing a subcutaneous tumor

A 3-month old immunodeficient nude mouse (Nu/Nu) weighing about 18 g was used for this study. Human cancer cells (A431 cell line) were subcutaneously injected on the right flank of the mouse. The injected cells were grown for 20 days resulting in a tumor size of about 10 mm in diameter. Then two imaging sessions were performed: before (control experiment) and

31 hours after NP injection. A NP solution of 200  $\mu\text{L}$  was injected intravenously via a tail vein. The amount of gold in the 200  $\mu\text{L}$  NP solution was 400  $\mu\text{g}$ . During imaging sessions, the mouse was anesthetized with a combination of isoflurane (0.5 ~2.0%) and oxygen (0.5 L/min). After the second imaging session, the mouse was euthanized by carbon dioxide ( $\text{CO}_2$ ) asphyxiation, and the tumor was excised for histological analysis (i.e., silver staining). All these procedures were performed under the animal protocol approved by Institutional Animal Care and Use Committee (IACUC) at The University of Texas at Austin.

### 2.3. *In vivo* imaging system

A 3-D US and PA imaging system developed for *in vivo* mouse imaging is shown in Fig. 2. A tunable laser system consisting an optical parametric oscillator (OPO) (PremiScan, Spectra-Physics) pumped by Q-switch Nd:YAG laser (Quanta-Ray PRO-Series, Spectra-Physics) was capable of producing 7 ns pulses at 10 Hz pulse repetition frequency. The overall spectral range of the system was from 400 to 2300 nm wavelength. For this study, we used 6 wavelengths ranging from 740 to 840 nm with an increment of 20 nm (i.e., 740, 760, 780, 800, 820, and 840 nm). The diameter of round-shaped Gaussian laser beams was consistently 12 mm for all wavelengths, and the maximum laser fluence for all wavelengths was 25  $\text{mJ}/\text{cm}^2$  satisfying an American National Standards Institute (ANSI) limit (i.e.,  $\sim 30 \text{ mJ}/\text{cm}^2$ ) [18]. The pulse-to-pulse laser energy was monitored and recorded using a laser power meter (Nova II, OPHIR)—the power meter readings were then used to compensate for laser energy variation during off-line PA image reconstruction.

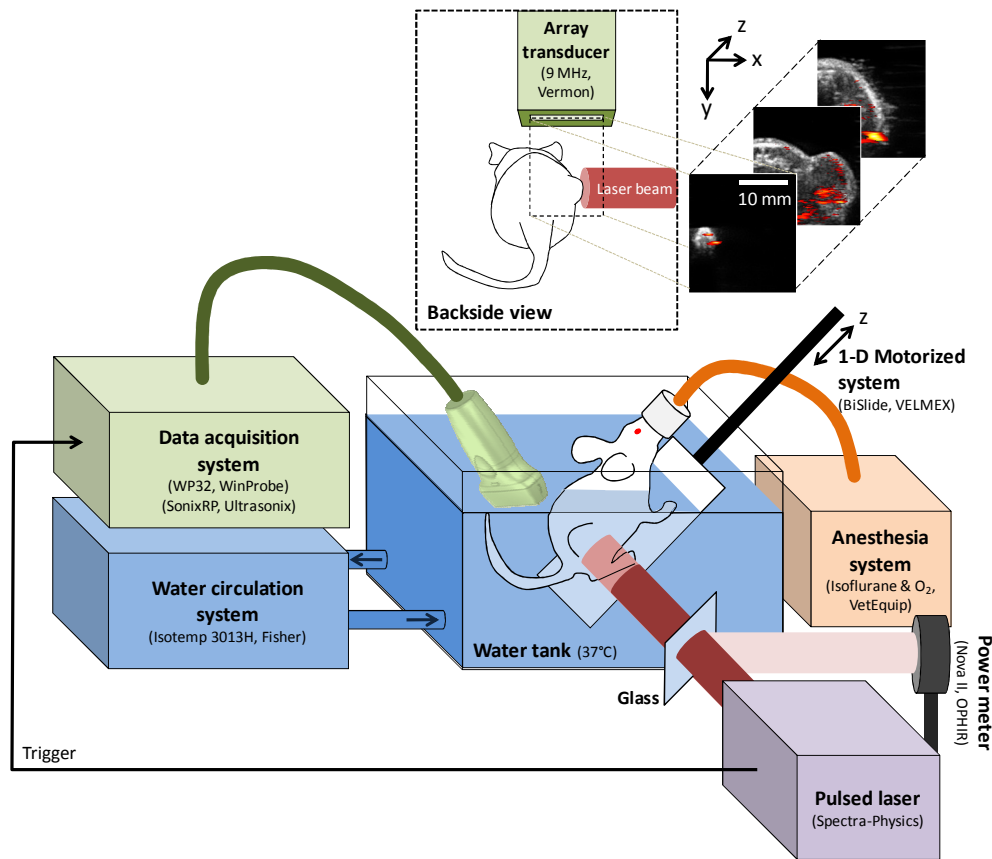


Fig. 2. Schematic diagram of the developed *in vivo* three-dimensional ultrasound and photoacoustic imaging system.

A water tank was used for acoustic coupling between the linear array transducer and the skin of the mouse and for maintaining the body temperature of anesthetized mouse. Water temperature was kept at 37°C during experiments using a water circulation system (Isotemp 3013H, Fisher). In order to keep both a transducer-cable connection and the mouse head above water, we constructed an imaging platform to diagonally secure the mouse. The imaging platform was connected to a 1-D motorized system (BiSlide, VELMEX) to scan the mouse for 3-D imaging.

Two systems—SonixRP by Ultrasonix, Inc., and WP32 by WinProbe, Inc.—were used for US and PA imaging, respectively. The SonixRP system was chosen for US imaging because of its ability to quickly capture high quality US images with multiple focal zones, while the WP32 system allowed simultaneous access to 32 channel data needed for fast PA imaging. Both systems were interfaced with the same linear array transducer (L12/128 by Vermon, 128 elements, 9 MHz center frequency, 5.8 MHz bandwidth) to collect either pulse-echo US or PA signals. For one 2-D US image, 128 beams of radiofrequency (RF) signals (i.e., beamformed US data) were collected using 64 transmit- and 32 receive-channels, requiring acquisition time of about 0.025 seconds. In PA imaging mode, 4 laser pulses were required for one full data set of 128 RF signals (i.e., pre-beamformed PA signals). Moreover, to enhance signal-to-noise ratio (SNR), 32 PA pre-beamformed RF signals were averaged requiring 128 laser pulses for one PA image. The acquisition time for one frame of PA image was 12.8 seconds. The PA image reconstruction (or, in other words, beamforming) was performed off-line.

#### 2.4. Spectroscopic photoacoustic imaging

##### Photoacoustic imaging

The collected PA signal was first filtered using a 128th order finite impulse response (FIR) bandpass filter. The cutoff frequency of the filter was determined based on the measured bandwidth of the transducer (9 MHz center frequency and 5.8 MHz bandwidth). Then the 32 bandpass filtered PA signals from each element were averaged in order to enhance SNR. The PA images were reconstructed using a delay-and-sum beamforming [19]. Specifically, the 128 PA signals were used to generate 96 scanlines or beams (i.e., beamformed data) covering a 96-element aperture positioned in the middle of the array. A Hamming window was applied for aperture apodization during the beamforming. This suppressed side-lobes of the PA beam, enhancing contrast-to-noise ratio (CNR) while widening a main lobe, and thus slightly degrading lateral spatial resolution. The PA beamformed RF data were down-converted by taking the absolute values of Hilbert transform of RF data. The PA images were then displayed using a linear scale.

##### Depth- and wavelength-dependent fluence compensation of photoacoustic signal

Assuming both stress and thermal confinements are satisfied, the PA maximum pressure,  $p_0$ , at the pressure source can be expressed as follows [20]

$$p_0(\lambda, \mathbf{r}) = \Gamma(\mathbf{r})\mu_a(\lambda, \mathbf{r})F(\lambda, \mathbf{r}), \quad (1)$$

where  $\Gamma$  is the local ( $\mathbf{r}$ ) Grüneisen parameter,  $\mu_a$  is wavelength ( $\lambda$ ) dependent local ( $\mathbf{r}$ ) optical absorption coefficient, and  $F$  is wavelength-dependent local laser fluence. Both the optical absorption coefficient and the Grüneisen parameter are tissue-dependent. The Grüneisen parameter is defined by the volume expansion coefficient ( $\beta$ ), the speed of sound ( $v_s$ ) and the heat capacity at constant pressure ( $C_p$ )

$$\Gamma = \frac{\beta v_s^2}{C_p}. \quad (2)$$

The distribution of the laser fluence depends on optical properties of the tissue and laser light delivery system (e.g., beam profile, incident laser fluence, etc.).

In this study, wavelength-dependent local fluence was estimated using the approach presented in Fig. 3 (steps 1-3). First, the imaged tissue was segmented by tissue type. Specifically, skin and background tissue were identified and skin thickness was determined from US images (Fig. 3, step 1). Then, using Beer's law, the fluence was estimated using a simple 2-D skin-tissue two-layer model (Fig. 3, step 2)

$$F(\lambda, \mathbf{r}) = F_0(\lambda) e^{-\mu_{eff}(\lambda, \mathbf{r})|\mathbf{r}|}, \quad (3)$$

where  $F_0$  is wavelength-dependent incident fluence measured by a laser power meter during experiments,  $|\mathbf{r}|$  is the distance between skin and position,  $\mathbf{r}$ , within the tissue, and  $\mu_{eff}$  is both wavelength- and tissue-dependent effective attenuation coefficient defined as

$$\mu_{eff} = \sqrt{3\mu_a(\mu_a + \mu_s)}, \quad (4)$$

where  $\mu_a$  and  $\mu_s$  are absorption and transport scattering coefficients, respectively. The optical properties of mouse skin and tumor were obtained from literature [21,22]. Finally, PA signal was compensated using the derived fluence map (Fig. 3, step 3). Note that the analysis described by steps 1-3 was performed for every optical wavelength resulting in wavelength- and depth-dependent fluence compensation of PA signal.

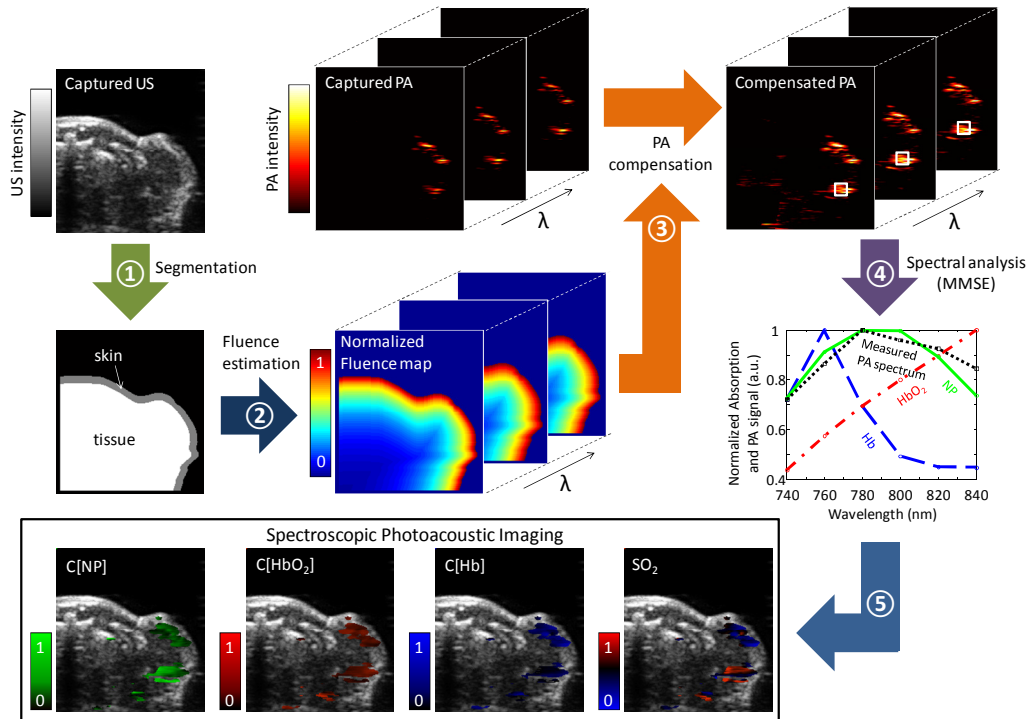


Fig. 3. Schematic diagram of the developed spectroscopic photoacoustic imaging algorithm.

### Spectral analysis

Assuming there are three major optical absorbers in a body (i.e., oxyhemoglobin (HbO<sub>2</sub>), deoxyhemoglobin (Hb), and nanoparticle (NP)), the absorption coefficient of localized mouse tissue can be defined by the sum of absorption coefficients for HbO<sub>2</sub>, Hb, and NP in the region. Note that the absorption coefficient ( $\mu_a$ ) is the product of the molar absorption coefficient ( $\epsilon$ ) and the molar concentration ( $C$ ) of the absorber. Therefore, the wavelength-dependent local absorption coefficient (i.e.,  $\mu_a(\lambda, \mathbf{r})$ ) can be described as

$$\mu_a(\lambda, \mathbf{r}) = C_{HbO_2}(\mathbf{r})\varepsilon_{HbO_2}(\lambda) + C_{Hb}(\mathbf{r})\varepsilon_{Hb}(\lambda) + C_{NP}(\mathbf{r})\varepsilon_{NP}(\lambda), \quad (5)$$

where  $C_{HbO_2}$ ,  $C_{Hb}$ , and  $C_{NP}$  are the molar concentrations [M] of HbO<sub>2</sub>, Hb, and NP, respectively, and  $\varepsilon_{HbO_2}$ ,  $\varepsilon_{Hb}$ , and  $\varepsilon_{NP}$  are the molar absorption coefficients [cm<sup>-1</sup>M<sup>-1</sup>] of HbO<sub>2</sub>, Hb, and NP, respectively. Given depth- and wavelength-dependent fluence compensation, the measured local PA spectrum ( $p_0(\lambda, \mathbf{r})$ ) can be directly related to the local absorption spectrum ( $\mu_a(\lambda, \mathbf{r})$ ) (see Eq. (1)). Linear least squares (LLS) method can resolve the concentrations of multiple absorbers, and therefore distinguish tissue components [12]. Moreover, the resolved HbO<sub>2</sub> and Hb concentrations can be used for estimating oxygen saturation in blood. However, the LLS method often predicts negative concentrations due to imperfect fluence compensations, noise in the measurements, contribution to PA signals from other optical absorbers, etc. Because a negative concentration has no physical meaning, it negates the calculated concentrations of the other absorbers at that location.

To overcome the problems of the LLS method for *in vivo* deep penetration imaging, we have developed a robust, less noise-sensitive PA spectral analysis algorithm that minimizes the mean square error while maintaining positive concentrations for each absorber (Fig. 3, step 4). Each molar absorption spectrum ( $\varepsilon(\lambda)$ ) of HbO<sub>2</sub>, Hb, and NP within the used wavelength range ( $\lambda_1 < \lambda < \lambda_2$ ) was first normalized as

$$\varepsilon^*(\lambda) = \frac{\varepsilon(\lambda)}{\max[\varepsilon(\lambda)]_{\lambda_1 < \lambda < \lambda_2}}. \quad (6)$$

Then the local absorption spectrum ( $\mu'_a(\lambda, \mathbf{r})$ ) can be described as

$$\mu'_a(\lambda, \mathbf{r}) = C[HbO_2](\mathbf{r})\varepsilon_{HbO_2}^*(\lambda) + C[Hb](\mathbf{r})\varepsilon_{Hb}^*(\lambda) + C[NP](\mathbf{r})\varepsilon_{NP}^*(\lambda), \quad (7)$$

where  $C[HbO_2]$ ,  $C[Hb]$ , and  $C[NP]$  are the contribution levels of the HbO<sub>2</sub>, Hb, and NP absorption spectra. By varying  $C[HbO_2]$ ,  $C[Hb]$ , and  $C[NP]$  from 0 to 1, and setting the sum of them to one (i.e.,  $0 < C[HbO_2], C[Hb], C[NP] < 1$  and  $C[HbO_2] + C[Hb] + C[NP] = 1$ ), the local absorption spectrum of all possible combinations of HbO<sub>2</sub>, Hb, and NP contributions at a position  $\mathbf{r}$  can be reconstructed into  $\mu'_a(\lambda, \mathbf{r})$ . Then  $\mu'_a(\lambda, \mathbf{r})$  is normalized in order to compare it with the normalized local PA spectrum (i.e.,  $p_0^*(\lambda, \mathbf{r})$ ) in a mean square error (MSE) sense:

$$MSE = E \left[ \left( p_0^*(\lambda, \mathbf{r}) - \mu_a'^*(\lambda, \mathbf{r}) \right)^2 \right]. \quad (8)$$

Note that local PA intensity was defined by averaging PA signals inside a kernel (500  $\mu$ m axially, 500  $\mu$ m laterally, and 500  $\mu$ m elevationally). The kernel size was selected to be larger than axial and lateral spatial resolutions of PA images. The values of  $C[HbO_2]$ ,  $C[Hb]$ , and  $C[NP]$  in Eq. (7) were numerically determined by minimizing the mean square error (MSE) of Eq. (8). Then minimum mean square errors (MMSEs) were used for reliability of the results.

The main difference between our MMSE method and the LLS method is that we allow constraints to be placed on the solution. However, the solutions from each approach are the same if the solution of the LLS method already satisfies the constraints. In addition, the MMSE method is a numerical approach, and thus computationally intensive while the LLS method has an analytical solution, and benefits from fast computation. Therefore, we used the numerical method only if the solution of the LLS analysis has negative values. By combining both approaches, we achieved the development of a fast, and less noise-sensitive spectroscopic PA imaging algorithm.

In this study, the MMSE of 0.005 was used for the threshold of the results. This is quite a strong constraint for reasonable analysis. The contribution levels of HbO<sub>2</sub>, Hb, and NP (i.e.,  $C[HbO_2]$ ,  $C[Hb]$ , and  $C[NP]$ ) were then used for visualizing the distributions of each. In order to estimate oxygen saturation (SO<sub>2</sub>) of blood, the following equation was used:

$$SO_2 = \frac{C_{HbO_2}}{C_{HbO_2} + C_{Hb}} = \frac{C[HbO_2]}{C[HbO_2] + nC[Hb]}, \quad (9)$$

where  $n$  is the scaling factor defined as

$$n = \frac{\max[\varepsilon_{HbO_2}(\lambda)]_{\lambda_1 < \lambda < \lambda_2}}{\max[\varepsilon_{Hb}(\lambda)]_{\lambda_1 < \lambda < \lambda_2}}. \quad (10)$$

Note that  $\varepsilon_{HbO_2}^*$  to  $\varepsilon_{Hb}^*$  ratio is no longer the same as  $\varepsilon_{HbO_2}$  to  $\varepsilon_{Hb}$  ratio (see Eq. (6)), and therefore a scaling factor needs to be considered to calculate the molar concentrations.

Figure 3 summarizes the developed spectroscopic PA imaging algorithm consisting of depth- and wavelength-dependent fluence compensation and spectral analysis of PA signal.

### 2.5. Histological analysis (silver staining)

To confirm the result of spectroscopic PA imaging, especially concentration of NPs ( $C[NP]$ ) after the injection, the mouse was euthanized and tumor was excised right after the second imaging session (i.e., 31 hours after NP injection) for histological analysis. The excised tumor was carefully marked for location and orientation of spectroscopic PA imaging planes. A total of 4 evenly distributed histological slides were made, and silver stained to identify depositions of gold NPs. Since silver staining has enhanced contrast to gold in bright-field microscopic images, we used silver staining slides to visualize the distribution of gold NPs in the tumor. The corresponding 2-D images of NPs in tissue ( $C[NP]$ ) were compared with silver stained tissue slides.

## 3. Results

Comparison of linear least square (LLS) and minimum mean square error (MMSE) methods is presented in Fig. 4. The US image (Fig. 4(a)) was used to generate a 2-D skin-tissue two-layer structure for the laser fluence compensation. As an example, the compensated PA image at 800 nm is shown in Fig. 4(b). Since the LLS method generates negative concentration values (Fig. 4(c)), some areas with strong PA signal are not mapped with optical absorbers (Fig. 4(d)). By applying the developed MMSE method, however, NP concentration can be reliably reconstructed (Fig. 4(e)). White arrows in Fig. 4(e) indicate locations and concentrations of NPs missed by LLS method, but recovered by MMSE method. Therefore, the developed spectroscopic PA imaging algorithm based on MMSE analysis can reconstruct the concentrations of optical absorbers in the region where LLS method fails due to negative concentration of photoabsorbers.

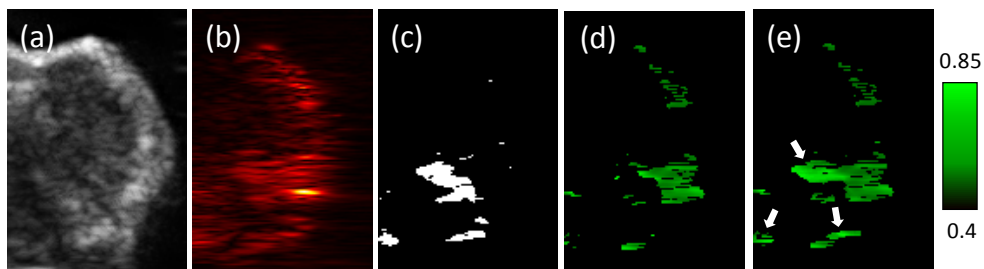


Fig. 4. Comparison between linear least square (LLS) and minimum mean square error (MMSE) methods. Ultrasound image (a) was used for the skin-tissue segmentation. The fluence compensated photoacoustic image (b) at 800 nm is shown as a reference. Spectral analysis based on LLS method can produce negative concentrations (c) of optical absorbers due to imperfect fluence compensations, noisy measurements, etc. The regions producing a negative NP concentration by LLS method get removed from the NP image. (d). However, the developed MMSE method can reliably reconstruct spatial distribution and concentration of NP: white arrows in panel (e) indicate locations where NP concentrations were recovered using MMSE method.

The spectral analysis based on MMSE method was applied to identify presence and concentration of major photoabsorbers in mouse tumor *in vivo*. The 3-D US images show mouse tumor morphology (i.e., tumor size and location) as well as overall outline of the mouse body. Tumor growth during the 31 hours between the two imaging sessions was recognizable in the 3-D US images presented in Fig. 5(a) and Fig. 5(g).

Single-wavelength PA images obtained at 800 nm (Fig. 5(b) and Fig. 5(h)) show optical absorption contrasts in the mouse body. Since we compensated PA signals based on local fluence changes estimated from a 2-D skin-tissue two-layer model, the color intensity on the images is proportional to the optical absorption of tissue (assuming that Grüneisen parameters of tissues are the same, see Eq. (1)). Within the tumor region, the PA signal distribution before and after the NP injection is significantly different. The increased PA signal generation is most likely due to NP deposition in the tumor. However, such a conclusion must be verified because PA signal increase could also be due to tumor growth and angiogenesis over 31 hours, or slight changes in the US and PA system setup and positioning of the mouse.

The spectroscopic PA imaging analysis shows the Hb, HbO<sub>2</sub>, and NP contributions to the PA signal. As expected, significant increase of NP concentration in the tissue was observed by comparing the C[NP] images before and after NP injection (Fig. 5(f) and Fig. 5(l), respectively). Clearly, plenty of NPs injected through tail vein accumulate at the tumor region. Moreover, Hb concentration is shown in tail vein area (Fig. 5(k)) which indirectly proves the validity of the developed spectroscopic PA image reconstruction algorithm. In addition, using Eq. (9) and estimates of C[Hb] and C[HbO<sub>2</sub>], oxygen saturation (SO<sub>2</sub>) of the blood can also be calculated (Fig. 5(c) and Fig. 5(i)).

Four cross-sections of tumor, indicated by dotted lines in the photograph of the mouse (Fig. 6(a)), were analyzed for correlation between PA-derived images and histological slides. Overall, the distribution of NPs in C[NP] images (Fig. 6(b)) and silver stain in histological slides (Fig. 6(c)) is well correlated. For example, the first and second cross-sections of the tumor have much fewer NPs than cross-sections 3 and 4—both C[NP] images and silver stained slides indicate the same trend. The enlarged regions of silver stained slides (Fig. 6(d) and Fig. 6(e)) clearly show NP accumulation at the tumor.

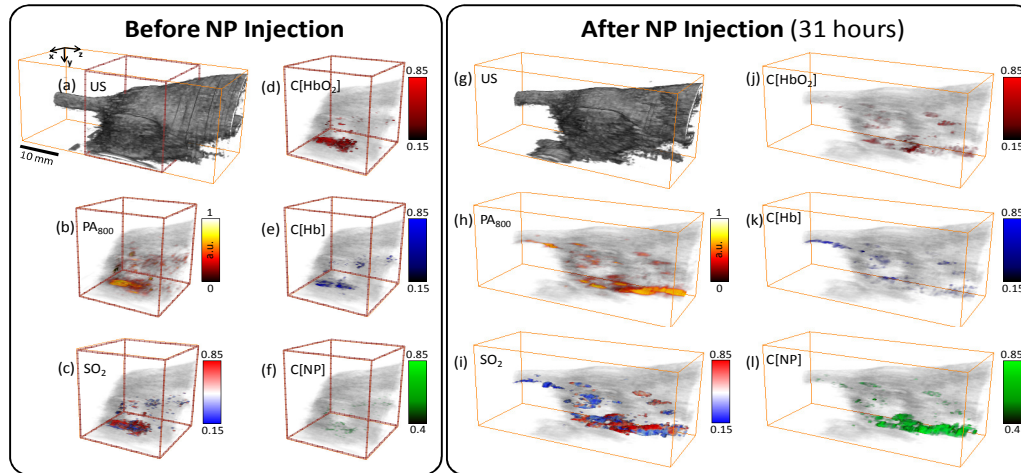


Fig. 5. Three-dimensional ultrasound images (panels a,g), photoacoustic images (panels b,h), and PA-derived oxygen saturation images (SO<sub>2</sub>, panels c,i), and images of oxyhemoglobin (C[HbO<sub>2</sub>], panels d,j), deoxyhemoglobin (C[Hb], panels e,k), and nanoparticle (C[NP], panels f,l) concentration before and 31 hours after tail vein injection of PEGylated gold nanorods into tumor bearing mouse. PA and PA-derived images are shown with ultrasound images in the background. Oxygen saturation was calculated using the concentrations of oxyhemoglobin and deoxyhemoglobin. Furthermore, anatomical features of the tumor (i.e., tumor size and location) are better shown in rotating 3-D images: ultrasound (panel g, Media 1), 3-D photoacoustics (panel h, Media 2), oxygen saturation (panel i, Media 3), and nanoparticle concentration (panel l, Media 4).

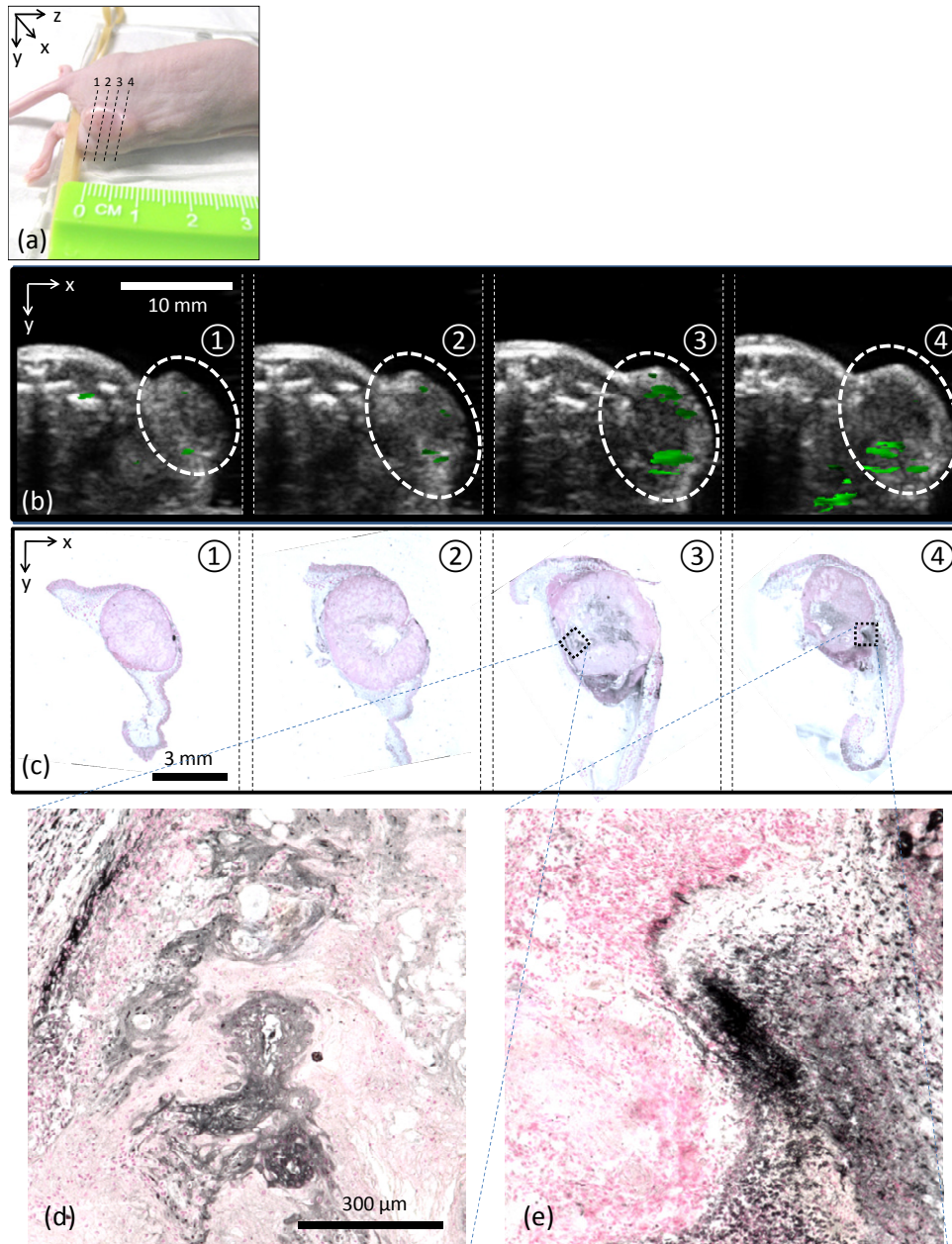


Fig. 6. (a) Photograph of the mouse with dotted lines indicating the approximate location of imaging planes and corresponding histological slides. (b) PA-derived maps of NP concentration displayed over the ultrasound images of the tumor. (c) Silver stained tissue slides where gray to black colors indicate presence of NPs. The enlarged areas of silver stained slides are shown in panels (d) and (e).

#### 4. Discussion

Spectroscopic PA imaging algorithm incorporating depth- and wavelength-dependent fluence compensation and hybrid LLS/MMSE analysis (Fig. 3) was developed and demonstrated using 3-D US and PA *in vivo* imaging (Fig. 2) of tumor bearing mouse injected with

PEGylated gold nanorods (Fig. 1). The results of spectroscopic PA imaging were verified using silver staining of the excised tumor tissue.

Before NP injection, spectroscopic PA imaging should detect no NPs. However, very small concentrations of NPs in a few locations were observed in image before the injection of NPs (Fig. 5(f)). Several factors may have an influence here. For example, it was assumed that PA signal is due to three types of optical absorbers: HbO<sub>2</sub>, Hb, and NPs. However, other absorbers may also be present resulting in some false positive. Noise in the measurements (or low signal-to-noise ratio of PA signal) can also result in incorrect analysis of optical absorbers contributing to PA signal. In addition, imperfect fluence compensations can cause spectral mismatch between the compared and reconstructed spectra.

The depth- and wavelength-dependent fluence compensation of PA signal can be further improved. In this work, we could not fully compensate wavelength-dependent local fluence changes due to the lack of information about optical properties of mouse tumor at different wavelengths. For more accurate fluence-dependent PA compensation, optical properties of various tissues at different wavelengths, measured independently and summarized to a look-up table, may be used. In addition, more sophisticated models, such as a 2-D or even a 3-D multi-layer model with incident beam specifications (e.g., beam diameter and intensity profile, incident angle, etc.), can improve local fluence estimation using a Monte Carlo simulation [23,24].

The developed spectroscopic PA imaging system and algorithms can identify NP delivery *in vivo*. The NPs that we used in the current studies were not specifically targeted to cancer cells. Therefore, the main mechanism of delivery was the enhanced permeability and retention (EPR) effect. However, the approach presented here can be applied to monitor the delivery of NPs and the temporal and spatial interactions of molecular specific targeted NP with tissue [25,26].

## 5. Conclusion

We have developed a more robust and less noise-sensitive spectroscopic PA imaging algorithm based on minimum mean square error (MMSE). The 3-D US and PA imaging system and developed algorithm were used for monitoring the delivery and accumulation of PEGylated gold nanorods which were intravenously injected into the mouse bearing a subcutaneous tumor. After the injection, spatial distribution of NPs within the tumor was successfully imaged using the US and PA imaging system and MMSE algorithm. Furthermore, NPs were reliably distinguished from the blood. Moreover, silver staining of tissue slices confirmed deposition of NPs in the tumor. Good correlation of NP distribution between histological slides and spectroscopic PA images was also demonstrated. The results of our study suggest that spectroscopic PA imaging can be used for monitoring the delivery and spatial distribution of plasmonic NPs *in vivo*.

## Acknowledgments

All authors thank Mrs. Pratixa Joshi and Mr. Neil Patodia for preparing A431 cells, Mr. Angel Zubieta for inoculating the cells into a mouse, Mrs. Janye O'Neal for the tail vein injection of nanoparticles, and TherapeUTex at The University of Texas at Austin for performing tissue histology. This work was supported by the National Institutes of Health under grants CA149740 and EB008101.